ADVANCED ENERGY MATERIALS
www.advenergymat.de

Nonequilibrium Pathways during Electrochemical Phase Transformations in Single Crystals Revealed by Dynamic Chemical Imaging at Nanoscale Resolution

*Young-Sang Yu, Chunjoong Kim, Yijin Liu, Anton van der Ven, Ying Shirley Meng, Robert Kostecki, and Jordi Cabana**

The energy density of current batteries is limited by the practical capacity of the positive electrode, which is determined by the properties of the active material and its concentration in the composite electrode architecture. The observation in dynamic conditions of electrochemical transformations creates the opportunity of identifying design rules toward reaching the theoretical limits of battery electrodes. But these observations must occur during operation and at multiple scales. They are particularly critical at the single-particle level, where incomplete reactions and failure are prone to occur. Here, operando full-field transmission X-ray microscopy is coupled with X-ray spectroscopy to follow the chemical and microstructural evolution at the nanoscale of single crystals of $Li_{1+x}Mn_{2-x}O_4$, a technologically relevant Li-ion battery electrode material. The onset and crystallographic directionality of a series of complex phase transitions are followed and correlated with particle fracture. The dynamic character of this study reveals the existence of nonequilibrium pathways where phases at substantially different potentials can coexist at short length scales. The results can be used to inform the engineering of particle morphologies and electrode architectures that bypass the issues observed here and lead to optimized battery electrode properties.

1. Introduction

Redox reactions provide an opportunity to convert or store energy to power our increasingly technological society. In turn, phase transformations in solids and their reversibility are key to many functionalities.[1–4] This reversibility is typically linked to the specific mechanism, which, in turn, can be affected by kinetic limitations, such as those imposed by solid-state transport. An extreme example is the need to move electrons and ions within the structure of a battery electrode active material.[4] The electrochemical energy thus stored is directly proportional to the amount of charge that can be exchanged reversibly. The larger the mass changes due to the extraction of ions, the more extensive the transformations, which can induce failure through fracture.[5] While engineering the electrode architecture has produced impressive means to compensate mechanical damage, this strategy typically induces losses in energy density by reducing the volumetric concentration of active material.[6] Strain can also prevent full, rapid, and reversible material utilization, leading to additional energy and power losses.

Understanding the kinetics of a phase transformation and its pathways, and coupling with the possible mechanical consequences is critical to identifying rules for materials with ultimate functionality. This understanding involves visualization of changes at the level of single crystals with the highest resolution possible. An extensive number of tools is nowadays available to scientists to define phase transformations at a variety of length scales. Of particular importance to the problem at hand are those coupling chemical probes, such as spectroscopy or diffraction, with microscopy. Further, while valuable insight can be achieved with experiments carried out ex situ, i.e., using samples recovered at different reaction stages, given the critical role of kinetics, protocols for visualization under working conditions are a priority. In the context of battery science, the impressive development of in situ transmission electron microscopy (TEM),[7,8] provides avenues to define phenomena that used to be achievable only through computational models.[9] However, spatially resolved, direct chemical speciation remains

Dr. Y.-S. Yu, Dr. C. Kim, Dr. R. Kostecki, Prof. J. Cabana
Environmental Energy Technologies Division
Lawrence Berkeley National Laboratory
Berkeley, CA, 94720, USA
E-mail: jcabana@uic.edu
Dr. Y.-S. Yu, Prof. Y. S. Meng
Department of NanoEngineering
University of California San Diego
La Jolla, CA, 92121, USA
Dr. C. Kim, Prof. J. Cabana
Department of Chemistry
University of Illinois at Chicago
845 W. Taylor St., Chicago, IL 60607, USA
Dr. Y. Liu
Stanford Synchrotron Radiation Lightsource
SLAC National Accelerator Laboratory
Menlo Park, CA 94025, USA
Prof. A. Van der Ven
Materials Department
University of California Santa Barbara
Santa Barbara, CA 93106, USA

DOI: 10.1002/aenm.201402040

challenging. In addition, to avoid the difficulties of using liquid electrolytes in a high-vacuum environment, which compromise the experimental resolution, the relevant reactions are often carried out in conditions that are far from what occurs in a battery, such as by strongly biasing a sample in contact with a Li metal tip with a thin layer of oxide.[10] Full-field transmission X-ray microscopy (FF-TXM) is a complementary tool capable of imaging a field of view (FOV) of about ≈25 µm at ≈25 nm spatial resolution in a single shot.[11,12] When coupled with X-ray absorption near-edge structure (XANES) spectroscopy at synchrotron sources, the morphology of a sample can be visualized with chemical sensitivity.[11,12] Using hard X-rays, redox-active species in most battery materials can be probed,[13,14] and the penetration capability enables investigations under operating conditions.[14,15]

This report presents the simultaneous chemical and morphological study, using operando FF-TXM-XANES at nanoscale resolution, of the electrochemical delithiation of single microcrystals of $Li_{1+x}Mn_{2-x}O_4$ (average composition of powder: $x \approx 0.05$), one of the state-of-the-art materials for Li-ion batteries.[16,17] All the phases in the compositional space show the same general reactivity versus Li, exemplified here for $LiMn_2O_4$,[16]

$$LiMn_2O_4 + Li^+ + e^- \rightarrow Li_2Mn_2O_4 \quad E_1 = 2.9\ V\ \ vsLi^+/Li_0 \qquad (1)$$

$$LiMn_2O_4 \rightarrow Li_{0.5}Mn_2O_4 + 0.5Li^+ + 0.5e^- \quad E_2 = 4.05\ V\ vs\ Li^+/Li^0 \qquad (2)$$

$$Li_{0.5}Mn_2O_4 \rightarrow Mn_2O_4 + 0.5Li^+ + 0.5e^- \quad E_3 = 4.15\ V\ vs\ Li^+/Li^0 \qquad (3)$$

Processes 1 and 3 follow first-order transitions (two-phase reaction), whereas reaction (2) is a second-order transformation (solid solution reaction) with complete miscibility between $LiMn_2O_4$ and $Li_{0.5}Mn_2O_4$. $Li_2Mn_2O_4$ presents a tetragonally distorted spinel structure, whereas all other phases are cubic. Only reactions (2) and (3) were found to be sufficiently reversible for electrochemical application. Strategies that enable durable cycling between $Li_2Mn_2O_4$ and Mn_2O_4 would result in capacities well above 200 mAh g^{-1}, the current limit in positive electrode materials.[17–19] Achieving this goal with crystal sizes at the microscale would minimize deleterious interfacial reactions,[20] as well as potentially increase the storage density of an electrode by avoiding poorly packed, porous nanopowders. Finally, understanding how a phase transformation proceeds in a crystal can provide guidance to engineers striving to reduce the amount of inactive materials such as conductive additives and binders so as to increase the energy density of a system.[21,22]

2. Results and Discussion

Operando FF-TXM-XANES (**Figure 1**a) was performed at beamline 6–2 at the Stanford Synchrotron Radiation Lightsource (SSRL) at the SLAC National Accelerator Laboratory (Menlo Park, USA).[11,12] During the electrochemical reaction, a series of images was recorded by sweeping across the X-ray absorption edge of Mn (Figure 1b). Single-pixel spectra were produced

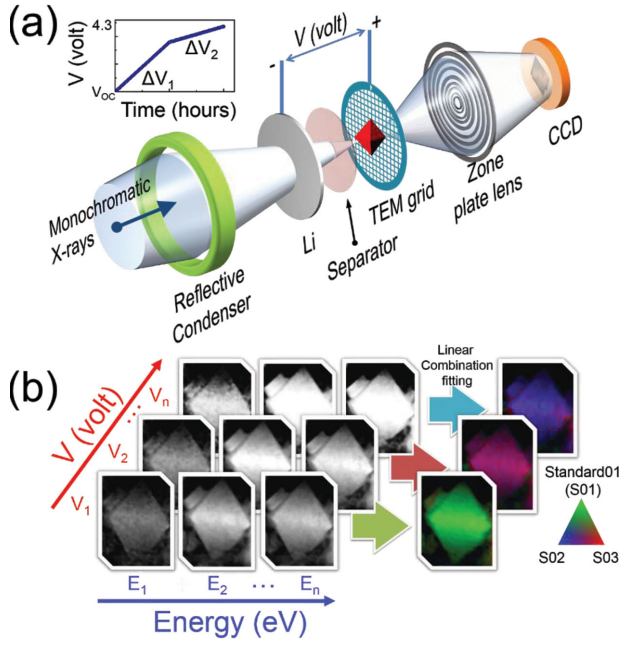

Figure 1. Experimental procedure for operando FF-TXM-XANES. a) Schematic illustration of the setup. A monochromatic hard X-ray beam is focused on the sample using an elliptical capillary and the image is projected by a Fresnel-type zone plate lens onto the charge-coupled device (CCD). The $Li_{1+x}Mn_{2-x}O_4$ ($x \approx 0.05$) particles were drop cast onto TEM grids, which were directly used as working electrodes. Electrochemistry was carried out using linear sweep voltammetry at two consecutive sweep rates, ΔV_1 and ΔV_2. b) Images were acquired at different X-ray photon energies (E) and cell potentials (V), and chemical maps were produced by fitting the corresponding XANES spectra of each pixel.

by integrating the intensity as a function of energy, and subsequently fitted using a linear combination (LC) of standards (see Experimental Section and Supporting Information for additional details). Morphological information was extracted at 6700 eV, where the absorption coefficients are practically independent of oxidation state (Figure S1a, Supporting Information). Critical to maximizing chemical resolution and contrast when observing small objects was the design of a cell that minimized absorption by components other than the active material, while preserving the conditions of a battery (see Experimental Section and Figure S2, Supporting Information). Instead of the thick metal foils commonly used in battery electrodes, a carbon-coated TEM grid was used as the current collector. This approach maximized chemical and morphological contrast while preserving electrochemical functionality. We were able to collect data in dynamic conditions, while the reaction was ongoing, which uncovered metastable states. Furthermore, we prepared faceted single crystals so as to directly infer crystallographic directionality from their morphology. The particles were dispersed onto the grid, and subsequently stabilized by depositing a thin Al film on the backside, which also ensured connection to the electrical circuit. While being considerably simpler than an actual battery, the proposed setup represents the electrochemical reactions taking place in a real device, and even reproduces some of its constraints. In an actual battery, carbon additives are typically used as the electronic connection between the particle and the current collector, and correspond

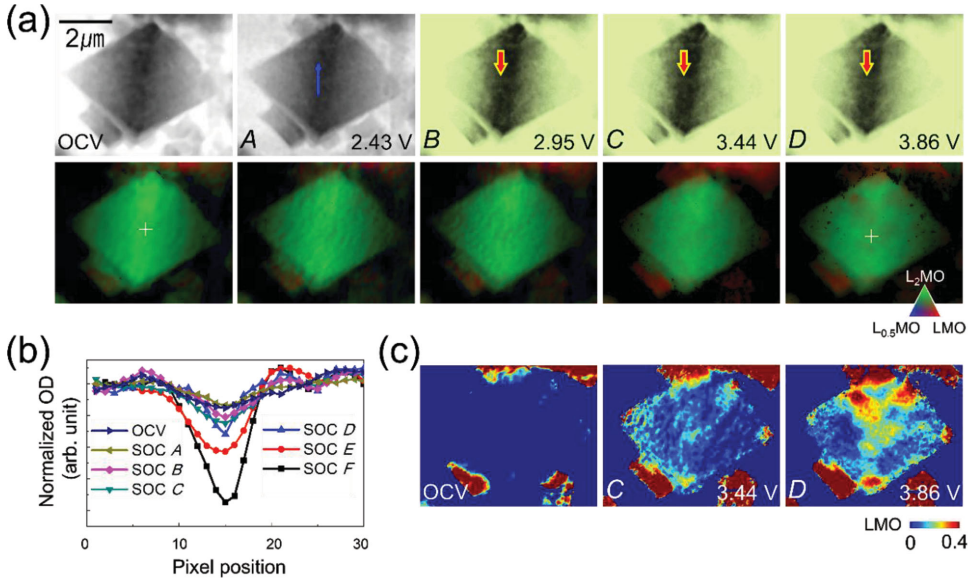

Figure 2. Chemical and morphological imaging of selected single octahedral spinel microcrystals during the tetragonal-to-cubic transition (reaction (1)). According to the chemical map, the initial state of these crystals was a tetragonal spinel rich in Mn^{3+}, i.e., $Li_{1+x+y}Mn_{2-x}O_4$, with y close to 1. a) Chemical and morphological maps at OCV and SOCs *A* to *D* for FOV I. The morphological maps (upper row) were collected from the inverted optical density (OD) images at 6700 eV. For SOCs *B*to *D*, contrast (+ 40%), brightness (+ 20%), and background color of the morphological maps were modified to enhance the visibility of cracks (red arrows). The potential of the cell at each SOC is also indicated (Figure S2b, Supporting Information). The chemical maps (lower row) were fit with L_2MO, LMO, $L_{0.5}MO$, and MO, but the latter was found in negligible amounts (see text for details). As a result, red, green, and blue colors indicate LMO, L_2MO, and $L_{0.5}MO$, respectively. Representative fits of single-pixel (white crosses in the chemical maps) spectra are shown in Figure S6 (Supporting Information). b) Dependence with SOC of the normalized OD across the line scans indicated by the blue arrow in (a). To reduce noise, 20 line profiles across the crack position were averaged. c) Maps depicting the contents in LMO at the indicated SOCs.

to 10% or less of the mass of the electrode.[22] At these levels and especially considering that active material powder is present in aggregated form during electrode assembly, the points of contact between the carbon and the active material are limited. In other words, a single-active particle is not equally connected to the circuit. The situation is similar in our setup, as each individual microcrystal sitting on the current collector has one point of contact to the current collector. This point of contact can span a whole crystal facet, given that the octahedron can gravitationally tend to fall on them. Therefore, as in an actual battery, parts of the crystal can be hundreds of nanometers away from the electronic connection.

Considering the spatial resolution of FF-TXM, single-crystal sizes of more than 1 μm were synthesized following a molten salt route.[23] The final sample was largely composed of $Li_{1.05}Mn_{1.95}O_4$, but also contained small amounts of the tetragonal spinel $Li_{2+x}Mn_{2-x}O_4$ (see Experimental Section) resulting from the large excess of lithium and low oxygen partial pressures in the chloride flux.[24] The crystals had an octahedral shape (Figure S3, Supporting Information), which is thermodynamically favored; each facet corresponds to the {111} family of lattice vectors.[25] Consequently, morphological observations contained crystallographic information. The electrochemical response of grids with a high loading of particles was comparable to conventional composite electrodes (compare Figure S4b to Figure S5a, Supporting Information). The electrochemical responses were significantly washed out but still observable in the FF-TXM-XANES experiment (Figures S2b and S5, Supporting Information) because the loading was reduced to ensure that areas existed with minimal particle overlap. These observations emphasize that our setup was successful in inducing the same electrochemical reactions as in standard cells for material testing. The as-made cells had an open-circuit voltage (OCV) around 2.5 V, as expected from the existence of $Li_{2+x}Mn_{2-x}O_4$, although the possibility of short circuiting during cell making could not be entirely discarded. These OCV values were consistent among a large number of cells assembled in this study.

The dynamics of the successive transformations during early stage of electrochemical deintercalation are illustrated in **Figures 2** and **3**. To minimize damage from continuous X-ray exposure and enhance the representativeness, chemical maps were sequentially collected in three different FOVs at specific states of charge (SOC). As a result, each snapshot for the same FOV was taken at intervals of roughly 60 min, i.e., in a noncontinuous manner. All single-pixel spectra were fit using bulk XANES data of the four discrete phases in reactions (1)–(3): tetragonal $Li_2Mn_2O_4$ (labeled L_2MO hereafter), cubic $Li_{1.05}Mn_{1.95}O_4$ (LMO), $Li_{0.6}Mn_{1.95}O_4$ ($L_{0.5}MO$), and $Li_{0.2}Mn_{1.95}O_4$ (MO). Pixels showing poor signal-to-noise ratios were filtered out.[26–28] Representative fits are presented in Figures S6 and S7 (Supporting Information); phase fractions could be estimated with *R*-factor of ≈0.0035. The accuracy of LC fit for the different FOVs is represented by *R*-factor maps in Figure S8 (Supporting Information). Around 90% of pixels (96.20% for the SOC *D*′ in FOV II) were fit with *R*-factors less than 0.02 (Figure S8c, Supporting Information). Given the complexity and sequence of phases involved in the transformation, the dataset was divided in two parts: during the tetragonal-to-cubic (reaction (1) above) and cubic-to-cubic transitions (reactions (2)

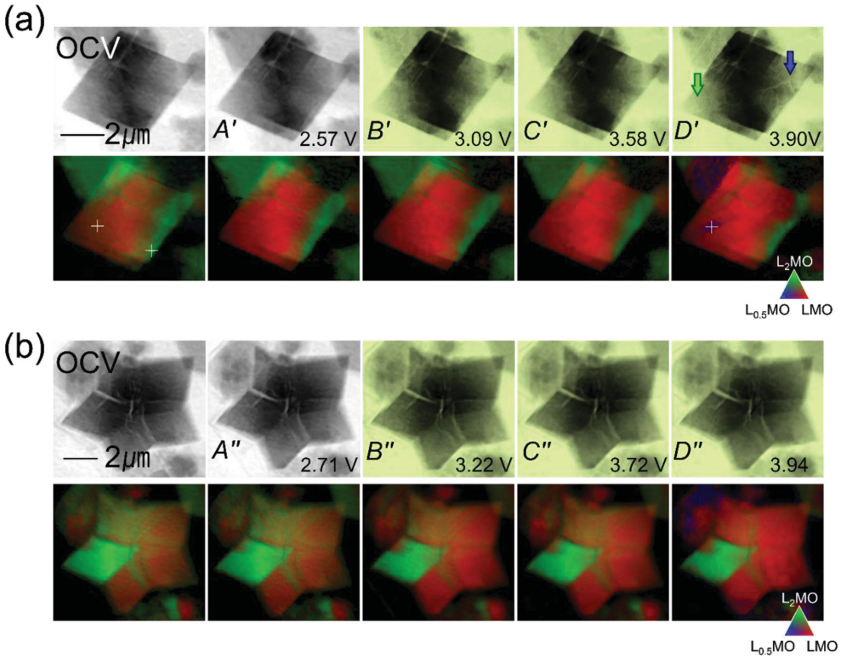

Figure 3. Chemical and morphological maps of FOVs of a) II and b) III during the tetragonal-to-cubic transition (reaction (1)). Inverted optical density images collected at 6700 eV (upper row) and chemical phase maps (lower row). For SOCs *B′* to *D′*, contrast (+ 40%) and background color of the morphological maps were modified to enhance the visibility of cracks (blue and green arrows). For SOCs *B″* to *F″*, only the background color of the morphological maps was modified. The potential of the cell at each SOC is also indicated (Figure S2b, Supporting Information). The chemical maps (lower row) were fit with L_2MO, LMO, $L_{0.5}MO$, and MO, but the latter was found in negligible amounts (see text for details). As a result, red, green, and blue colors indicate LMO, L_2MO, and $L_{0.5}MO$, respectively. Representative fits of single-pixel (white crosses in the chemical maps) spectra are shown in Figure S7 (Supporting Information).

and (3) above), occurring below and above 4.0 V, respectively. As expected, the maps collected during the tetragonal-to-cubic transition were found to contain negligible amounts of MO; the significance level was set as any pixel containing more than 1% of the standard (Figure S9, Supporting Information). Consequently, this standard was not represented in the corresponding chemical maps. Figure 2 represents data collected for FOV I during this transition, whereas Figure 3 contains FOVs II and III. Likewise, the L_2MO contents were negligible during the cubic-to-cubic transition, and, thus, were not represented in the corresponding chemical maps. As a result, in the maps corresponding to OCV and SOCs *A* to *D*, the presence of the L_2MO, LMO, and $L_{0.5}MO$ standards was assigned colors green, red, and blue, respectively. In turn, in SOCs *E* and *F*, red and blue indicated MO and $L_{0.5}MO$, whereas green was used with pixels containing LMO. In order to facilitate the interpretation of the complex images, maps where color contrast is proportional to the contents of a single compound are provided in Figure 2c.

The pristine state of the particle in FOV I (Figure 2a) was successfully fit solely with L_2MO (Figure S6a, Supporting Information). In the early stages of charging, areas containing LMO formed and propagated, but growth was localized at the tips and edges of the octahedron (SOC *C* in Figure 2). Subsequently, these domains continued to grow along the edges and surface of the crystal as the reaction proceeded (SOC *D*). Since the spectra represent an average over the thickness of the crystal (transmission mode), mixtures could result from incomplete delithiation along the direction of the X-ray beam. Similar phase growth could also be observed in FOVs II and III (Figure 3), which were already mixed compositions in their pristine state, possibly reflecting the overlithiated impurities observed by powder XRD. L_2MO-rich domains were found well above the potential for the tetragonal-to-cubic transition (at 2.9 V, compared with SOC *D*, at ≈3.8 V),[29] indicative of a sluggish transformation.

The high-resolution morphological imaging capabilities of FF-TXM-XANES also allowed us to establish a correlation between the chemical reaction and the appearance of microscopic defects (Figures 2 and 3). The localized formation of cubic domains within the particle in FOV I, which started as pure tetragonal phase, was concurrent with crack initiation in the crystal (see red arrows in Figure 2a, compared with the location of oxidized pixels in Figure 2c). Since nanocracks that are smaller than the detection limit of the tool (≈30 nm) would not be readily visible in the image, supporting evidence was extracted from line profiles of optical density at selected pixels (Figure 2b). The intensity profile over the line indicated in the figure (blue line in Figure 2a) decreased as the particle was cycled, and before SOC *D*, consistent with the onset of fracture during the tetragonal-to-cubic transition. Considering the crystallographic directions defined by crystal morphology, there was a systematic trend toward generation of cracks along planes parallel to <100> directions of the cubic spinel octahedra. The specific plane indices cannot be determined because the images obtained here are 2D projection over the sample volume along the beam path. Nonetheless, this observation would be in conflict with recent reports of fracture along the (111) planes.[30] Such fracture pattern would lead to a more complex pattern of optical mass density loss given the orientation of the particles in this study, and, thus, it should not cause the change in the line profile shown in Figure 2b. The directional growth of cracks could be attributed to the anisotropy between the tetragonal ($Li_{2+x}Mn_{2-x}O_4$, space group $I4_1/amd$) and cubic ($Li_{1+x}Mn_{2-x}O4$, space group $Fd\bar{3}m$) spinel lattices.[16] Due to the Jahn–Teller distortion of the MnO_6 octahedra, this transition brings about a 3% expansion along the a_T axis (*T* refers to the tetragonal structure) and 12% shrinkage in c_T axis, yielding a ≈5.6% anisotropic volume contraction.[16] The need to nucleate a phase with a large lattice mismatch along $(001)_T$ can introduce strain that causes local plastic deformation,[31] resulting in defects that tend to develop perpendicular to the direction of greatest mismatch,[32] where preferential fracture can occur.

The phase progression in FOV II was represented as an overlapped greyscale map in Figure S10 (Supporting Information), indicating the size of the domain that could be fit with at least 60% LMO. Growth of ca. 0.7 μm of the oxidized domain toward

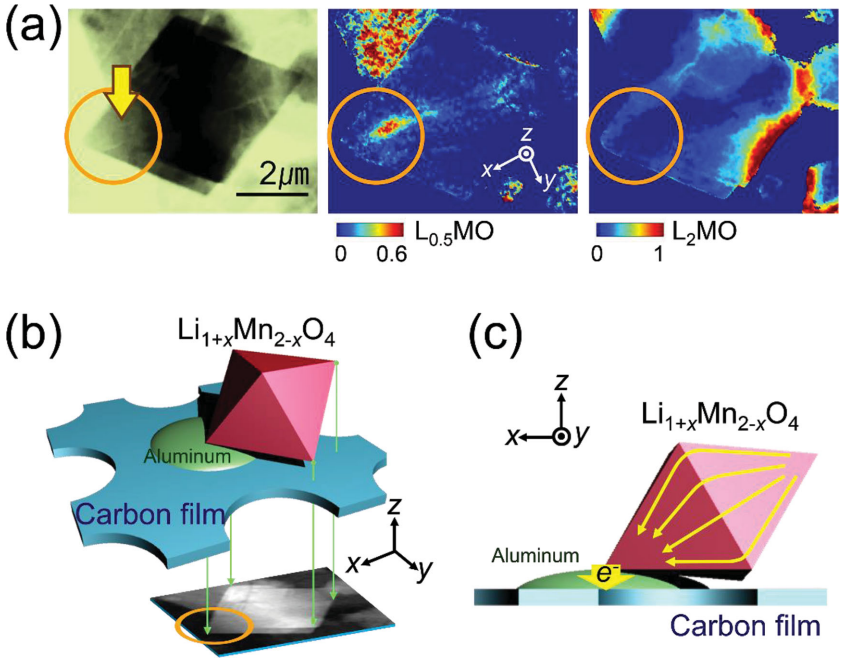

Figure 4. Nonequilibrium pathways of transformation. a) Distribution of phases at SOC *D′* in FOV II. (Left) Morphological image collected from the inverted optical density at 6700 eV, with modified contrast (+ 60%), brightness (–10%), and background color to enhance the visibility of cracks (yellow arrow). (Middle, Right) Maps indicating the ratios of $L_{0.5}MO$ and L_2MO, as indicated, in each pixel. Note that the scales correspond to the spectral fraction and its maximum is 0.6 (middle) and 1.0 (right). b) Schematic illustration of the experimental layout in FOV II, depicting the point of electrical contact between the crystal and the grid and Al film forming the current collector. The green arrows indicate the path of the X-ray beam, which results in the transmitted image. c) Proposed flow of electronic charge during the electrochemical reaction. Lateral view of (b) showing the flow of electrons due to contact only existing at one corner of the octahedron, indicated by orange circles in (a, middle) and (b). In parts where contact does not exist, electron flow must proceed through the oxide phase, leading to the nonequilibrium pathways of transformation in (a).

the overlithiated particle edges with potential was dynamically observed (see yellow arrow in Figure S10, Supporting Information). Strikingly, appearance of domains that could be fit including the $L_{0.5}MO$ standard was found on the opposite end of the crystal even before this propagation was complete, at 3.90 V (compare SOC *D′* in Figure 3a and **Figure 4**). These Mn^{4+}-rich domains appeared to emerge along an existing crack parallel to one of the {100} planes of the cubic spinel octahedron (see yellow arrow in Figure 4a). The correlation between the presence of a crack and an oxidized domain was less clear in other parts of the crystal. In contrast to the clear phase boundaries observed during the tetragonal-to-cubic transition, the concentration of oxidized domains gradually decreased away from the crack position. This oxidized phase formation led to the coexistence of two different compositional domains that are 1 V apart (see above) in the same crystal. This large gradient could be explained as due to inhomogeneities in electron transfer from the current collector, which is located behind the particle in the images (Figure 4b,c). In this scenario, the points of electrical contact between grid and particle would be concentrated on the Mn^{4+}-rich side (left side in the images), where transfer would be facile (Figure 4c). Propagation of the redox reaction toward the Mn^{3+}-rich end (right side) of the particle would depend on slow solid-state transport of both Li ions and electrons. It is also possible that the transformation is enhanced along cracks because of the increase of surface area for lithium transfer into the electrolyte.

Near 4.00 V (SOC *E* in **Figure 5**), the crystals were found to be compositionally homogeneous throughout; each single pixel could be fit to similar mixtures of $L_{0.5}MO$ and LMO (Figure S6c, Supporting Information). This homogeneity of mixed states was taken as indicative of the existence of solid solutions in reaction (2),[16] which corresponds to the redox process at ≈4.05 V in Figures S2b and S5 (Supporting

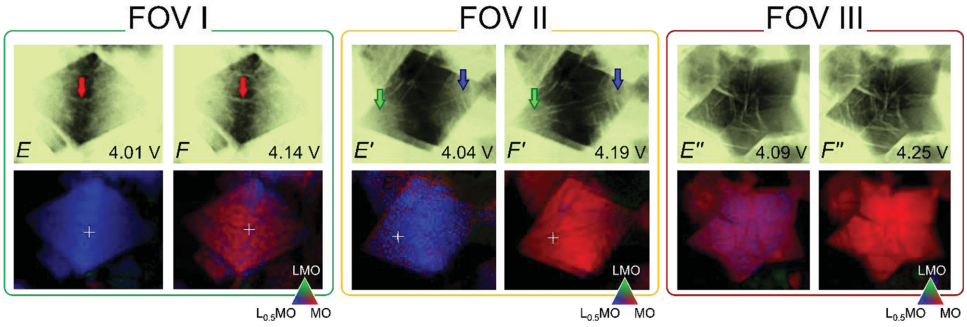

Figure 5. Chemical and morphological imaging of selected single octahedral microcrystals in $Li_{1+x}Mn_{2-x}O_4$ ($x \approx 0.05$) during the cubic-to-cubic transition (reactions (2) and (3). Two maps are provided for each FOV, as indicated. Morphological maps (upper row) were collected from the inverted optical density images at 6700 eV. Contrast, brightness, and background color of the morphological maps were modified to enhance the visibility of cracks (red, green, and blue arrows). The potential of the cell at each SOC is also indicated (Figure S2b, Supporting Information). The chemical maps (lower row) were fit with L_2MO, LMO, $L_{0.5}MO$, and MO, but L_2MO was found in negligible amounts (see text for details). As a result, red, green, and blue colors indicate MO, LMO, and $L_{0.5}MO$, respectively. Representative fits of single-pixel (white crosses in the chemical maps) spectra are shown in Figures S6 and S7 (Supporting Information).

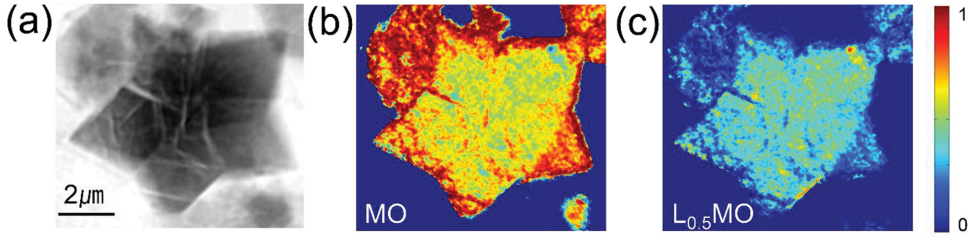

Figure 6. Preferential growth of MO along cracks in FOV III. a) Inverted optical density image of SOC *E″*, collected at image at 6700 eV. Heat maps where color contrast scales with the ratio of b) spectral standards MO and c) $L_{0.5}MO$ in each pixel (see Figure 5).

Information). This observation suggests that the oxidized domains in SOC *D′* were also in this second-order cubic-to-cubic transition. In thermodynamic conditions, solid solution transformations should occur homogeneously through an object. The compositional inhomogeneities that build in the $Li_{1+x}Mn_{2-x}O_4$ particle during delithiation from the overlithiated state highlight the nonequilibrium conditions imposed by solid-state transport during the electrochemical reaction, and the importance of operando measurements to accurately describe them.

Upon extensive lithium deintercalation (SOCs *F* as well as *E′*/*F′* and *E″*/*F″* in Figure 5), the crystals regained inhomogeneity, with pixels showing mixtures of $L_{0.5}MO$ and MO. This two phase coexistence could be clearly visualized in compositional maps of a single standard (MO and $L_{0.5}MO$ in **Figure 6** and Figure S11, Supporting Information). The inhomogeneity during this first-order cubic-to-cubic transition (reaction (3)) was found to be less pronounced than in the tetragonal-to-cubic (reaction (1)). In general, the trend was for highly oxidized pixels to accumulate along the rims (for instance, see SOC *E′* in Figure 5 and S11, Supporting Information), and subsequently grow toward the interior as the reaction proceeded (SOC *E″* in Figures 5 and 6), suggesting that the reaction initiated at all surfaces. We also found evidence that cracking occurred and/or was significantly enhanced during cubic-to-cubic transitions (see green arrows in Figures 3a and 5, and optical density line scans in Figure 2b). Although this transformation is isotropic, the total volume change from LMO to MO is in the order of 6 to 7%.[16] The change is still predicted to be enough to result in fracture, particularly in large crystals, such as here, and at high rates of reaction.[33–35] Fracture was extensive, and again found to be preferential along the octahedron axes (Figures 3 and 5). The position and shape of the emerged MO phase bore some correlation with the location of the cracks (see FOV III in Figure 6). It could be envisaged that a crack provides access to fresh surfaces through which the phase transformation can proceed.[26,36]

3. Conclusion

In summary, this FF-TXM-XANES study successfully probed successive compositional transitions within a single microcrystal of $Li_{1+x}Mn_{2-x}O_4$, at nanoscale spatial resolution. Specifically, we visualized the close correlation between chemistry and mechanics, and revealed the origins of cracking in $Li_{1+x}Mn_{2-x}O_4$ ($x \approx 0.05$) both during tetragonal-to-cubic and cubic-to-cubic transitions. Such cracking prevents both utilization of the whole compositional domain and the design of Li-ion battery electrodes formed of large crystals, both of which raise the energy density of a battery through different mechanisms. The directionality of the cracks can inform the design of crystals that bypass these failure mechanisms, and, hence, support optimum function even in the full compositional range and at large particle sizes.[37] The methodology proposed here will be extended to other spinel samples that are modified by means of elemental substitution and/or coatings to improve performance,[19] in order to ascertain their effect on the phase transformation mechanism. It could further be applied to a variety of other battery-relevant materials following different mechanisms, identify failure modes and build general descriptions of interplay of charge transport, chemistry, and mechanics in active particles. It further expands the versatility of high-resolution spectromicroscopy to reveal complex multiscale phenomena in materials, which could enable rational pathways toward technological solutions in a variety of applications.

4. Experimental Section

Full-Field Transmission X-ray Microscopy: FF-TXM was performed at the 54 pole wiggler beamline (BL 6–2) at the SSRL, SLAC National Accelerator Laboratory, Menlo Park, CA (USA).[37] The TXM routinely operates in absorption contrast mode over a wide energy range from 5 to 14 KeV with spatial and energy resolutions of ≈30 nm and $\Delta E/E = 10^{-4}$, respectively. The energy of the X-rays is controlled using a liquid nitrogen-cooled, double crystal monochromator. The X-rays with selected energy are then focused onto the sample by an elliptically shaped capillary condenser providing a FOV of approximately 25 × 25 μm^2. The microscope then uses a Fresnel zone plate as objective lens for achieving a magnification of about 50×. With the position being adjusted as the energy was tuned, the zone plate projects the transmission image onto a charge-coupled device (CCD) while maintaining focus at each given energy. For the operando measurements, 2D XANES images (0.5 s exposure time, five repetitions, binning 2, 1024 × 1024 pixels) were collected from 6500 to 6700 eV in 53 steps at specific charging state. In order to eliminate distortions in flux and small beam instabilities, simultaneous acquisition of reference images through an open or outside area of the sample were performed at each energy and charging state (0.5 s exposure time, 15 repetitions, binning 2, 1024 × 1024 pixels). The repetitions in the exposures were performed for improving the dynamic range of the existing CCD and, subsequently, for increasing the signal to noise ratio in the data. The XANES measurement for a single FOV was accomplished in 50 min.

Design of the Cell for Operando FF-TXM-XANES: All *operando* electrochemical experiments were performed in modified 2032 coin cells with lithium metal foil as counter electrode, with one disk of Celgard 2400 soaked in a 1 M $LiPF_6$ solution in ethylenecarbonate:dimethyl carbonate (45:55 v:v) as separator and electrolyte, respectively.

Schematic illustrations of the operando cell are shown in Figure S2 (Supporting Information). To ensure sufficient transparence to the X-ray beam, holes were punched in the cell cases. $Li_{1+x}Mn_{2-x}O_4$ ($x \approx 0.05$) crystals were dropcast onto 20 nm thick holey-carbon-film-coated Au TEM grids (QUANTIFOIL R3.5/1, Quantifoil Micro Tools GmbH), which were directly used as working electrodes in Li metal half cells. To prevent particle movements and make electrical connection stable during X-ray measurements, a 3 μm-thick Al film was deposited onto the backside of TEM grids by DC-magnetron sputtering under a base pressure of 1.0×10^{-5} Torr. Subsequently, unattached particles were washed out with acetone and ethanol. The inset in Figure S2 (Supporting Information) shows a representative scanning electron microscopy image of the final sample. In order to prevent contaminations during cell cycling, after cell assembly, the holes in the cell cases were completely sealed with 1 μm thick X-ray transparent Si_3N_4 widows (Silson Ltd.) by applying vacuum epoxy (Torr Seal, Varian Inc.). All cell assembly and sample manipulation was performed in an Ar-filled glovebox. Owing to the high X-ray transmittance of all the cell components employ in this study, which were light and very thin, especially when compared with widely used operando cell support and sealing materials such as pouch bags and Kapton tape windows,[21] high-quality images with high resolution can be acquired while preserving the electrochemical function of the crystals (Figures S2b and S5, Supporting Information). Such properties were confirmed in cells were the grids were saturated with crystals, using cyclic voltammetry at 50 μV s^{-1} between 3.0 and 4.5 V. Anodic and cathodic doublets were observed near 4.0 V versus Li^+/Li^0, as expected based on literature data.[16] The FF-TXM-XANES operando cell contained a much smaller amount of particles than in these test environments in order to minimize particle overlap, but weak features at the same electrochemical potentials could still be detected in some cases, Figures S2b and S5d (Supporting Information).

Image Data Processing: Because the focal length of the Fresnel zone plate varies with incident X-ray energy, the magnification factor and alignments between imaged FOVs are changed at different energies. In addition, the sample stage movements to record reference images at each energy cause misalignments owing to the limitation of the motor performance. Therefore, bicubic interpolations and a phase correlation algorithm[38] were implemented for magnification corrections and automatic image registration, respectively. After initial image processing, the transmittance changes of each pixel as a function of energy was converted to XANES spectra, which were fit with LC of standard spectra using a least square method. From the pixel-by-pixel LC fitting results, the ratios of chemical species can be used to generate a RGB map of the FOV. The quality of each LC fit can be checked with the *R*-factor[28,39] defined as, $R = \sum(\text{data-fit})^2 / \sum(\text{data})^2$. All data processing, including reference correction, averaging, magnification correction, image registration, XANES reconstruction, and fitting, was performed using the TXM-Wizard software.[28]

Synthesis of $Li_{1+x}Mn_{2-x}O_4$ ($x \approx 0.05$): Pristine $Li_{1+x}Mn_{2-x}O_4$ ($x \approx 0.05$) was synthesized through a modified molten salt method. All chemicals were purchased from Sigma-Aldrich (purity level ≥ 97%). Stoichiometric amounts of $Mn(NO_3)_2{\cdot}4H_2O$ were dissolved in a minimum amount of deionized water with a LiCl:KCl flux (molar ratio 0.68:0.32, m.p. 425 °C). The molar ratio between the flux and the manganese was fixed at 70. The dissolved mixture was mixed in a mortar, dried at 80 °C for 2 h, and then heated to 650 °C in a covered alumina crucible at a rate of 3 °C min^{-1}. After holding at 650 °C for 8 h, the mixture was cooled at the same rate. The powder was washed with de-ionized water, filtered and dried at 60 °C overnight. The resulting dry particles were employed as a seed for a second molten salt treatment in identical conditions to favor grain growth. X-ray diffraction patterns for the seed and final crystals were acquired using a Bruker D8 Discover X-ray diffractometer operating with Cu Kα radiation (λ_{avg} = 1.5418 Å), and can be found in Figure S4a (Supporting Information). The pattern could be fully indexed with a phase-pure cubic spinel structure ($Fd\bar{3}m$ space group) with a = 8.22(1). The cell parameter is consistent with a slight Li excess in $Li_{1+x}Mn_{2-x}O_4$, estimated to be $x \approx 0.05$ based on previous studies of this phase diagram.[36] A shoulder at lower angles (see arrow in Figure S4a, Supporting Information) was indicative of the formation of small amounts of the tetragonal spinel $Li_{2.05}Mn_{1.95}O_4$, resulting from the large excess of lithium and low oxygen partial pressures in the chloride flux.[24] Data resulting from in depth characterization of this material can be found as Supporting Information.

Supporting Information

Supporting Information is available from the Wiley Online Library or from the author.

Acknowledgements

This work was supported as part of the NorthEast Center for Chemical Energy Storage (NECCES), an Energy Frontier Research Center funded by the U.S. Department of Energy, Office of Science, Basic Energy Sciences under Award # DE-SC0012583. The TXM at SSRL was supported by the NIH/NIBIB under grant number 5R01EB004321. SSRL is supported by the DOE-BES. The authors would like to thank Dr. Hugues Duncan (LBNL) for technical advice with the $Li_{1+x}Mn_{2-x}O_4$ synthesis and Dr. Weilun Chao (LBNL) for his assistance with cell fabrication.

Received: November 14, 2014
Published online: December 22, 2014

[1] K. Otsuka, X. Ren, *Prog. Mater. Sci.* **2005**, *50*, 511.
[2] A. Llordes, G. Garcia, J. Gazquez, D. J. Milliron, *Nature* **2013**, *500*, 323.
[3] Z. Yang, C. Ko, S. Ramanathan, *Annu. Rev. Mater. Res.* **2011**, *41*, 337.
[4] A. Van der Ven, J. Bhattacharya, A. A. Belak, *Acc. Chem. Res.* **2012**, *46*, 1216.
[5] W. H. Woodford, W. C. Carter, Y.-M. Chiang, *Energy Environ. Sci.* **2012**, *5*, 8014.
[6] B. P. N. Nguyen, S. Chazelle, M. Cerbelaud, W. Porcher, B. Lestriez, *J. Power Sources* **2014**, *262*, 112.
[7] J. Y. Huang, L. Zhong, C. M. Wang, J. P. Sullivan, W. Xu, L. Q. Zhang, S. X. Mao, N. S. Hudak, X. H. Liu, A. Subramanian, H. Fan, L. Qi, A. Kushima, J. Li, *Science* **2010**, *330*, 1515.
[8] M. T. McDowell, S. W. Lee, J. T. Harris, B. A. Korgel, C. Wang, W. D. Nix, Y. Cui, *Nano Lett.* **2013**, *13*, 758.
[9] F. Wang, H.-C. Yu, M.-H. Chen, L. Wu, N. Pereira, K. Thornton, A. Van der Ven, Y. Zhu, G. G. Amatucci, J. Graetz, *Nat. Commun.* **2012**, *3*, 1201.
[10] Y. Zhu, J. W. Wang, Y. Liu, X. Liu, A. Kushima, Y. Liu, Y. Xu, S. X. Mao, J. Li, C. Wang, J. Y. Huang, *Adv. Mater.* **2013**, *25*, 5461.
[11] J. C. Andrews, S. Brennan, C. Patty, K. Luening, P. Pianetta, E. Almeida, M. C. H. van der Meulen, M. Feser, J. Gelb, J. Rudati, A. Tkachuk, W. B. Yun, *Synchrotron Radiat. News* **2008**, *21*, 17.
[12] J. C. Andrews, B. M. Weckhuysen, *Chem. Phys. Chem.* **2013**, *14*, 3655.
[13] J.-D. Grunwaldt, C. G. Schroer, *Chem. Soc. Rev.* **2010**, *39*, 4741.
[14] M. Ebner, F. Marone, M. Stampanoni, V. Wood, *Science* **2013**, *342*, 716.
[15] J. Wang, Y.-c. K. Chen-Wiegart, J. Wang, *Nat. Commun.* **2014**, *5*, 4570.
[16] T. Ohzuku, M. Kitagawa, T. Hirai, *J. Electrochem. Soc.* **1990**, *137*, 769.
[17] J. B. Goodenough, Y. Kim, *Chem. Mater.* **2009**, *22*, 587.
[18] C. Wu, *MRS Bull.* **2010**, *35*, 650.
[19] H. K. Noh, H.-S. Park, H. Y. Jeong, S. U. Lee, H.-K. Song, *Angew. Chem. Int. Ed.* **2014**, *53*, 5059.
[20] B. L. Ellis, K. T. Lee, L. F. Nazar, *Chem. Mater.* **2010**, *22*, 691.

[21] W. Lai, C. K. Erdonmez, T. F. Marinis, C. K. Bjune, N. J. Dudney, F. Xu, R. Wartena, Y.-M. Chiang, *Adv. Mater.* **2010**, *22*, E139.
[22] H. Zheng, R. Yang, G. Liu, X. Song, V. S. Battaglia, *J. Phys. Chem. C* **2012**, *116*, 4875.
[23] E. K. Akdogan, R. Brennan, M. Allahverdi, A. Safari, *J. Electroceram.* **2006**, *16*, 159.
[24] V. Berbenni, A. Marini, *J. Anal. Appl. Pyrolysis* **2002**. *62*, 45.
[25] A. Karim, S. Fosse, K. A. Persson, *Phy. Rev. B* **2013**, *87*, 075322.
[26] U. Boesenberg, F. Meirer, Y. Liu, A. K. Shukla, R. Dell'Anna, T. Tyliszczak, G. Chen, J. C. Andrews, T. J. Richardson, R. Kostecki, J. Cabana, *Chem. Mater.* **2013**, *25*, 1664.
[27] F. Meirer, J. Cabana, Y. Liu, A. Mehta, J. C. Andrews, P. Pianetta, *J. Synchrotron Rad.* **2011**, *18*, 773.
[28] Y. Liu, F. Meirer, P. A. Williams, J. Wang, J. C. Andrews, P. Pianetta, *J. Synchrotron Rad.* **2012**, *19*, 281.
[29] M. M. Thackeray, Y. Shao-Horn, A. J. Kahaian, K. D. Kepler, E. Skinner, J. T. Vaughey, S. A. Hackney, *Electrochem. Solid-State Lett.* **1998**, *1*, 7.
[30] X. Hao, X. Lin, W. Lu, B. M. Bartlett, *ACS Appl. Mater. Interfaces* **2014**, *6*, 10849.
[31] J. Park, W. Lu, A. M. Sastry, *J. Electrochem. Soc.* **2011**, *158*, A201.
[32] D. Hull, D. J. Bacon, *Introduction to Dislocations*, 4th Ed., Butterworth-Heinemann, Boston **1986**.
[33] W. H. Woodford, Y.-M. Chiang, W. C. Carter, *J. Electrochem. Soc.* **2013**, *160*, A1286.
[34] J. Christensen, J. Newman, *J. Electrochem. Soc.* **2006**, *153*, A1019.
[35] D. J. Miller, C. Proff, J. G. Wen, D. P. Abraham, J. Bareño, *Adv. Energy Mater.* **2013**, *3*, 1098.
[36] J. M. Paulsen, J. R. Dahn, *Chem. Mater.* **1999**, *11*, 3065.
[37] A. Van der Ven, K. Garikipati, S. Kim, M. Wagemaker, *J. Electrochem. Soc.* **2009**, *156*, A949.
[38] B. S. Reddy, B. N. Chatterji, *IEEE Trans. Image Process.* **1996**, *5*, 1266.
[39] B. Ravel, M. Newville, *J. Synchrotron Rad.* **2005**, *12*, 537.